ROYAL SOCIETY OF CHEMISTRY

PAPER

Check for updates

MoSe₂-based room temperature gas sensor with a sub-parts-per-billion limit for ammonia and *N,N*-dimethylformamide†

Virendra Singh Choudhary,[a] Ramandeep Singh,[a] Ashok Kumar, [ID][a] C. S. Yadav,[b] Sandeep Sharma, [ID][d] Joel Garcia [ID]*[c] and Surender Kumar Sharma [ID]*[a]

A limit of detection of toxic gases at the level of ppb is critical for industrial safety. Here, we designed a room temperature MoSe₂-based sensor for dual detection of ammonia (NH_3) and *N,N*-dimethylformamide (DMF). The $MoSe_2/TiO_2$ composite exhibits a rapid and highly selective response to both NH_3 and DMF compared to other industrial analytes. The $MoSe_2/TiO_2$ heterostructures exhibit a band gap of 0.31 eV, highlighting their electronic structure, adsorption energy, and fundamental gas sensing mechanism. NH_3 and DMF demonstrated robust spontaneous adsorption on the below-$MoSe_2$ surface, exhibiting the lowest adsorption energy (-0.12 eV) and (-0.09 eV) of NH_3 and DMF, respectively. Bader charge analysis revealed charge transfer from the gas molecule to the heterostructure surface, enhancing its conductivity and gas detection sensitivity. The adsorption of NH_3 on the MoSe₂ site is exothermic whereas on the TiO_2 side it is endothermic, indicating the potential of $MoSe_2/TiO_2$ composites for efficient room-temperature gas sensing. The sensor achieved an 85% higher response to NH_3 and an 80% higher response to DMF, with density functional theory (DFT) simulations confirming a high negative adsorption energy. Detection limits were calculated at 4.91 ppb for NH_3 and 7.82 ppb for DMF under 40% relative humidity, with robust sensitivity across varying humidity levels. Response times were reasonably stable, with NH_3 detection at 150 s and recovery in 37–110 s, while DMF was detected in 150–160 s and recovered in 45–74 s. This study highlights the potential of the $MoSe_2/TiO_2$ composite in real-time, room-temperature monitoring of both NH_3 and DMF, making it a valuable tool for industrial safety and environmental monitoring without the need for external recovery mechanisms.

1. Introduction

In recent years, gas sensors have become widely used in various fields, including industrial production,[1] the automotive industry,[2] medical applications,[3] indoor air quality supervision,[4] and environmental monitoring.[5] These applications demand sensors that are sensitive and selective for specific gas analytes, as well as compact and easy to manufacture. Additionally, these sensors should operate at room temperature,[6] be energy-efficient, and be cost-effective

compared to existing technologies.[7] The emission of volatile organic compounds (VOCs) and hazardous gases has contributed to air quality degradation and poses significant risks to human health due to increasing gas pollution.[8] According to the World Health Organization, air pollution is a major contributor to illness and premature death, particularly in developing countries.[9]

Ammonia (NH_3) and *N,N*-dimethylformamide (DMF) are two common industrial chemicals that pose significant health risks.[10] NH_3 is a colorless gas with a pungent odor, produced by agricultural activities and industrial processes.[11] It is used in various applications like refrigeration systems, water purification, and household cleaning products. However, exposure to NH_3 can cause eye irritation, burns to the nose and throat, and, in severe cases, respiratory failure.[12,13] Due to its high volatility, detecting low concentrations of NH_3 is crucial for safety applications. DMF is widely used as a solvent in industries such as textiles and leather,[14] but exposure to DMF vapors can cause hepatotoxicity and cancer, and poses particular risks to

[a] Department of Physics, School of Basic Sciences, Central University of Punjab, Bathinda 151401, India. E-mail: surender.sharma@cup.edu.in

[b] Department of Physics, Indian Institute of Technology, Mandi, 175075, India

[c] Department of Chemistry, De La Salle University, Manila, Philippines. E-mail: joel.garcia@dlsu.edu.ph

[d] Department of Physics and Photonics Science, National Institute of Technology, Hamirpur, Himachal Pradesh 177005, India

pregnant women.[15] Thus, detecting DMF at low levels is equally important.

The development of faster, lower detection limit sensors has become a priority, with numerous methods being investigated,[16] including chemiresistive sensors,[17] which are favored for their simplicity, cost-effectiveness, and ease of integration.[18] Metal oxide semiconductors (MOSs) are commonly used in chemiresistive sensors due to their stability and high sensitivity to gases.[19] However, MOS-based sensors generally require high operating temperatures to achieve optimal gas responses,[20] leading to high energy consumption and complicated sensor designs.[21] Conducting polymers, which can operate at room temperature, have emerged as an alternative, but they suffer from stability issues and sensitivity degradation over time.[22]

Recent advancements in 2D materials, particularly transition metal dichalcogenides (TMDCs), such as MoS_2, $MoSe_2$, and WS_2, have brought new possibilities to gas sensing technologies.[23–25] TMDCs offer a large surface area, tunable electronic properties, and layer-dependent gas-sensing characteristics, making them ideal candidates for room temperature applications.[26] $MoSe_2$, in particular, has shown promise in detecting gases like NH_3, H_2S, and NO_2. However, challenges remain in achieving high selectivity and stability under humid conditions, a crucial factor for real-world applications in industries and environmental monitoring.[27,28]

In this study, we address these challenges by utilizing $MoSe_2/TiO_2$ composites for the dual detection of NH_3 and DMF at room temperature. By forming a heterostructure, we aim to enhance the sensitivity and selectivity of the sensor through their synergistic interaction. Unlike previous studies, which focused on high-temperature operation of TiO_2-based sensors, our work demonstrates effective room temperature operation, low detection limits, and stability under varying humidity conditions. As highlighted in Table S1 (ESI†), most existing sensors show diminished performance in humid environments,[29–33] whereas our sensor exhibits consistent performance, making it a viable candidate for real-world applications. This work presents a significant advancement in sub-parts-per-billion (ppb) gas detection for both NH_3 and DMF, addressing a critical need for low-cost, energy-efficient sensors that operate effectively under ambient conditions.

2. Experimental section

2.1 Materials

Pure selenium powder (Se), sodium molybdate dihydrate ($Na_2MoO_4 \cdot 2H_2O$), hydrazine hydrate, titanium(IV) isopropoxide $Ti[OCH(CH_3)_2]_4$, and sodium boro hydrate ($NaBH_4$) were purchased from Sigma-Aldrich, India, and used without any further purification.

2.2 Synthesis of the $MoSe_2/TiO_2$ nanocomposite

The $MoSe_2/TiO_2$ composite was synthesized by the hydrothermal method. The first step involved the synthesis of TiO_2. Initially, 20 mL of titanium(IV) isopropoxide was added

dropwise in DI-water and stirred continuously for 30 minutes to obtain a clear solution. The resultant solution was filtered with DI water and ethanol several times and dried at 65 °C. After collecting the white precipitates, the material was calcined at 500 °C for 2 hours in a tubular furnace and this way TiO_2 powder was obtained.[34] This procedure reliably produces ~ 1 g of TiO_2 powder per batch, and similar reproducibility was observed across multiple batches.

In the second step, the $MoSe_2/TiO_2$ composite was synthesized using a hydrothermal method. First, 200 mg of TiO_2 powder (obtained in the previous step) was bath-sonicated in 50 mL of distilled water to obtain a suspension of TiO_2. To this suspension, after adding 0.4 gm of selenium powder and 0.6 gm of sodium molybdate dihydrate, the resulting mixture was bath sonicated for 10 minutes. 0.2 g of $NaBH_4$ and 10 mL of hydrazine hydrate were added to the above mixture. The obtained mixture was bath-sonicated for an hour, and the resulting red-colored mixture was transferred into a 100 mL Teflon-lined stainless-steel autoclave. The autoclave was maintained at 200 °C in a furnace for 48 hours and then allowed to cool to room temperature naturally. After cooling, the black precipitates were collected by filtration using filter paper, followed by multiple washes with deionized water and ethanol. The final product was dried in a vacuum oven at 60 °C for 24 hours. This sample was designated as MT21 (~ 1.2 g). Subsequently, using an identical procedure but changing the weight ratio, two more samples were synthesized namely MT11 and MT12. More details can be found in Table S2 of the ESI.† It is to be noted that the same name was assigned to two terminal devices that were obtained from the respective composites.

2.3 Characterization of sensing materials

The structural and morphological characteristics of the pure and composite materials were examined using field emission scanning electron microscopy (FESEM) with a Merlin Compact model, which is equipped with energy-dispersive X-ray spectroscopy (EDX). The crystallinity of the materials was confirmed through X-ray diffraction (XRD) using a PANalytical Empyrean system and Cu-Kα radiation (wavelength: 1.54 Å). Raman spectroscopy was conducted with a RIMS-U-DC spectrometer that utilizes a 532 nm laser source. Additionally, X-ray photoelectron spectroscopy (XPS) analysis was performed using an ESCALAB instrument coupled with Omicron nanotechnology to determine the elemental composition and oxidation states of the materials.

2.4 Sensor fabrication and sensing measurements

To fabricate the sensing device, 10 mg of the dried $MoSe_2/TiO_2$ composite powder was combined with two to three drops of distilled water to create a uniform paste. This paste was then applied to an alumina substrate featuring gold electrodes spaced approximately 2 mm apart, using a paintbrush. Following the application of the sensing layer, the sensor was dried in a vacuum oven at 65 °C for 2 hours. A digital photograph of the two-terminal sensor device, measuring 1 cm × 1 cm, is provided in Fig. S1 (ESI†). Sensing measurements were conducted

using a homemade setup, details of which have been previously described in other studies.[33,35] The sensing measurements were performed at different natural relative humidity (RH) levels (40–80%), which were recorded using a digital hygrometer. Hence, the sensing measurements mimic the real-world situation. All VOC gases with variable concentration can be obtained by evaporation of pure ethanol, methanol, acetone, propanol, formaldehyde (40 wt%), N-methyl pyrrolidone (NMP), dimethylformamide (DMF) and ammonia (25 wt%) on a small hot plate placed at the corner of the test chamber. The known volume of the respective VOC was injected into the test chamber using a Hamilton microliter syringe. The required concentrations were calculated using eqn (1).[33,35]

$$C = \frac{22.4\rho\omega TVs}{273MV} \times 1000 \qquad (1)$$

In this equation, C represents the concentration of various gases in parts per million (ppm), ρ denotes the density of the concentrated liquid (g mL^{-1}), ω indicates the purity of the liquid, T signifies the temperature (K), Vs refers to the volume of the evaporated liquid (µL), M is the molecular weight of the liquid (g mol^{-1}), and V represents the volume of the test chamber (L).

2.5 Computational methodology

We investigated the gas sensing properties of MoSe$_2$/TiO$_2$ heterostructures, employing first principles calculations based on density functional theory (DFT). We utilized the Vienna *Ab Initio* Simulation Package (VASP) with the Perdew Burke–Ernzerhof (PBE) exchange–correlation functional and the generalized gradient approximation (GGA).[36–39] A substantial vacuum distance of 20 Å in the z-direction prevented interaction between two periodic images. Monkhorst–Pack k points of $8 \times 8 \times 1$ points were used to analyze the geometric optimization of the MoSe$_2$/TiO$_2$ heterostructure.[40] We employed the conjugate gradient method during the geometrical relaxation, with a plane-wave basis set and cutoff energy of 450 eV. The criteria for energy convergence were set at 10^{-4} eV.

3. Results and discussion

3.1 Structural characterizations

The XRD patterns of the MoSe$_2$/TiO$_2$ (1 : 1), MoSe$_2$/TiO$_2$ (1 : 2), and MoSe$_2$/TiO$_2$ (2 : 1) composites were obtained in the range of 10°–80°. The XRD patterns of TiO$_2$ calcined at 500 °C and MoSe$_2$ are also given for comparison, as shown in Fig. S2 (ESI†). The diffraction peaks of TiO$_2$ observed at 25.54°, 37.17°, 38.04°, 38.98°, 48.25°, 54.14°, 55.26°, 62.89°, 69.12°, 70.04°, and 75.30°, correspond to the (101), (103), (004), (112), (200), (105), (211), (204), (116), (220), and (215) crystal planes of the anatase phase of TiO$_2$ (JCPDS 73-1764), respectively.[41] Similarly, the diffraction peaks at 13.2°, 28.6°, 31.2°, 41.5°, 56.5°, and 65.3° correspond to the (002), (004), (100), (006), (008), and (108) planes, respectively, which are indexed to the hexagonal crystal structure of MoSe$_2$ (JCPDS 29-0914).[42,43] A few more peaks at 23.4°, 29.6°, 45.3°, 51.5°, and 61.6°
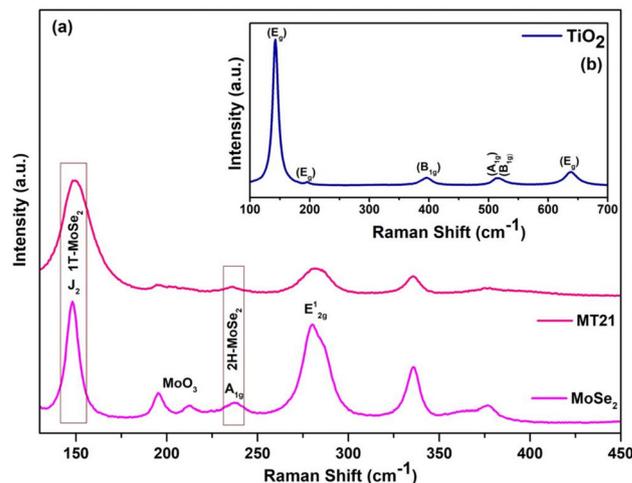

Fig. 1 Raman spectra of (a) MoSe$_2$ and the MoSe$_2$/TiO$_2$ (2 : 1) composite and (b) TiO$_2$.

corresponding to the (110), (130), (320), (410), and (160) planes confirm the presence of orthorhombic MoO$_3$ (JCPDS 35-0609). In the MoSe$_2$/TiO$_2$ composites, the diffraction peaks corresponding to TiO$_2$ and MoSe$_2$ are present with a minor phase of MoO$_3$, hence confirming the formation of a MoSe$_2$/TiO$_2$ composite with high purity. Fig. 1(a) shows the Raman spectrum of MoSe$_2$ with five dominant peaks clearly observed at 149, 241, 280.8, 336, and 378 cm^{-1}. Here, the peaks observed at 241 and 280.8 cm^{-1} correspond to the A$_{1g}$ and E$^1_{2g}$ modes of 2H-MoSe$_2$ and the peak corresponding to 378 cm^{-1} predicts the interlayer modes of vibration of the Mo and Se atoms.[44,45] Moreover, the additional resonance peaks in the as-prepared sample at 149 cm^{-1} have been identified as the J$_2$ phonon modes of 1T-MoSe$_2$. The peaks at 149 cm^{-1} and 196 cm^{-1} correspond to Se–Se bonding.[42] The peaks at 336 and 212 cm^{-1} have been attributed to the O–Mo–O bending in MoO$_3$.[35] The Raman spectrum of TiO$_2$ calcined at 500 °C is shown as an inset in Fig. 1(b). It matches with the anatase phase of TiO$_2$, which has six Raman active modes: E$_g$(1) (144 cm^{-1}), E$_g$(2) (197 cm^{-1}), B$_{1g}$(1) (399 cm^{-1}), A$_{1g}$/B$_{1g}$(2) (overlapped at 519 cm^{-1}), and E$_g$(3) (639 cm^{-1}).[46] The presence of the E$_g$(2) peak, which is usually very hard to detect, evidences the high degree of crystallinity of the samples. In the Raman spectrum of the MoSe$_2$/TiO$_2$ composite (MT21), the dominant peaks of MoSe$_2$ are observed at 241, 282, 336, and 378 cm^{-1} and the peaks of TiO$_2$ are observed at 146, 197, and 399 cm^{-1}, respectively. Certain peaks of TiO$_2$ have low intensity due to the larger content of MoSe$_2$ phase. Moreover, all MoSe$_2$ and TiO$_2$ peaks are observed in the expected region.

X-ray photoelectron spectroscopy (XPS) was employed to investigate the chemical states and electronic structure of MoSe$_2$, TiO$_2$, and the MoSe$_2$/TiO$_2$ composite (Fig. 2 and Fig. S4, S5, ESI†). Fig. S4 (ESI†) features the complete survey spectra, confirming the presence of molybdenum (Mo), selenium (Se), titanium (Ti), and oxygen (O) in the MoSe$_2$/TiO$_2$ composite. The high-resolution spectra for Mo 3d, Se 3d, Ti 2p, and O 1s are illustrated in Fig. 2(a)–(d). The Mo signal shown in Fig. 2(a) can
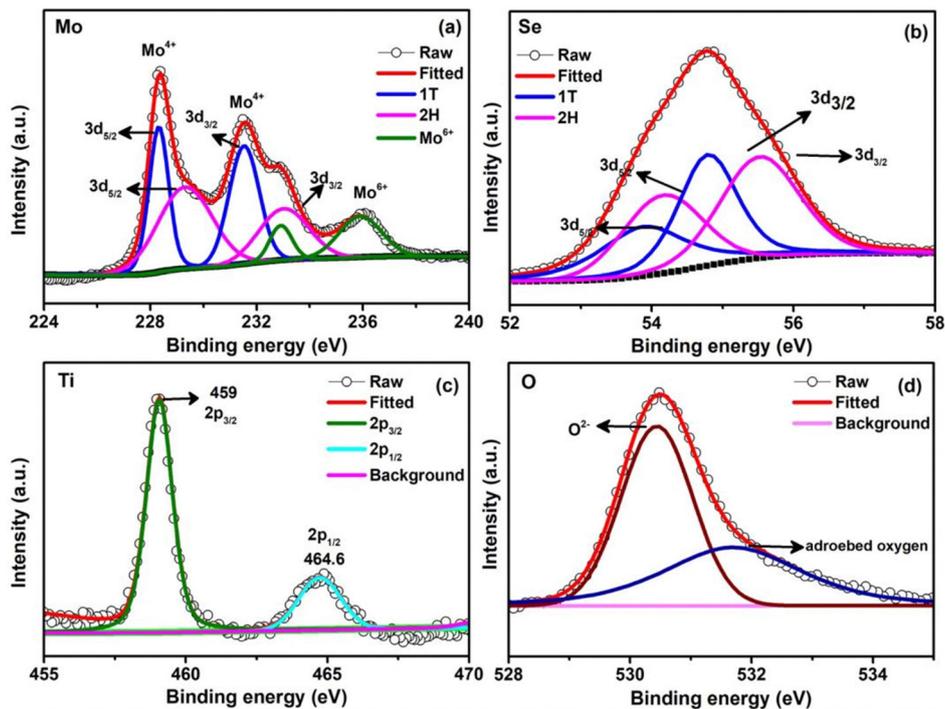
Fig. 2 XPS spectra of MoSe$_2$/TiO$_2$ (2 : 1) composites, including (a) Mo 3d spectrum, (b) Se 3d spectrum, (c) Ti 2p spectrum, and (d) O 1s spectrum.

be fitted into three sets of doublet peaks. The lower binding energy doublet peaks (231.4 eV for Mo 3d$_{3/2}$ and 228.3 eV for Mo 3d$_{5/2}$) correspond to the 1T-MoSe$_2$ phase.[47–49] The doublet peaks at medium binding energies (232.1 eV for Mo 3d$_{3/2}$ and 229 eV for Mo 3d$_{5/2}$) are associated with the 2H-MoSe$_2$ phase,[47–49] while the peaks at higher energies (235.7 eV for Mo 3d$_{3/2}$ and 232.6 eV for Mo 3d$_{5/2}$) are attributed to Mo in the +6-oxidation state.[50] This analysis indicates the presence of the 1T phase in the synthesized MoSe$_2$ sample. The Se 3d spectrum, shown in Fig. 2(b), exhibits a significantly broadened peak profile, which can be fitted into two sets of doublet peaks. The lower energy doublet (54.7 eV for Se 3d$_{3/2}$ and 53.7 eV for Se 3d$_{5/2}$) corresponds to the 1T phase, while the higher energy doublet (55.3 eV for Se 3d$_{3/2}$ and 54.3 eV for Se 3d$_{5/2}$) represents the 2H phase.[51] Fig. 2(c) displays the Ti 2p spectra, where two peaks at 458.8 eV and 464.5 eV are assigned to Ti 2p$_{3/2}$ and Ti 2p$_{1/2}$, respectively, confirming the presence of Ti^{4+} and indicating the dominant valence state of +4 for titanium in TiO$_2$. In the O 1s spectra shown in Fig. 2(d), peaks at 530.7 eV and 532 eV correspond to the oxygen-deficient structure of TiO$_2$ and the O^{2-} oxidation state in TiO$_2$, respectively.[51,52] Overall, the XPS analysis clearly indicates that the various samples contain traces of both 1T and 2H phases of MoSe$_2$. The individual MoSe$_2$ and TiO$_2$ XPS data are provided in Fig. S5 (ESI†).

3.2 Electrical and gas-sensing characteristics of the MoSe$_2$/TiO$_2$ composite

The electrical properties of the MoSe$_2$/TiO$_2$ composites and MoSe$_2$ are studied using current–voltage (I–V) measurements at room temperature and shown in Fig. S6(a) (ESI†). Both devices

exhibited linear curves in a fixed voltage range, suggesting their ohmic nature. This advocates that MoSe$_2$ and the MoSe$_2$/TiO$_2$ composite exhibit semiconducting properties.[13] Fig. S6(b) (ESI†) displays the I–V curves when a MoSe$_2$ based two-terminal device was exposed to three different concentrations of DMF (3, 10, 20 ppm) at 30 °C. With increased DMF concentration, the current level increases, indicating a decrease in device resistance in the presence of DMF. Almost similar behavior with increased current levels was displayed by the MoSe$_2$/TiO$_2$-based devices, thus indicating that the latter has improved sensitivity towards DMF. Due to their sensitivity towards DMF, the devices were also tested with different levels of ammonia (see Fig. S6, ESI† panels (d) and (e)). The MoSe$_2$-based devices have shown better sensitivity towards NH$_3$ than DMF. In panel (f), a joint comparison between two different analytes is displayed for MoSe$_2$/TiO$_2$. As clear from the data, the device exhibited superior detection of NH$_3$ than that of DMF at 30 °C. Therefore, it is clear that the devices exhibit ohmic behavior and selective behavior towards NH$_3$ and DMF. More detailed sensing measurements were performed with different levels of NH$_3$, as shown in Fig. 3. As we see, when a device (MoSe$_2$/TiO$_2$) is exposed to NH$_3$, its resistance decreases. And then after removal of NH$_3$ from the test chamber, the resistance again recovered to its initial value, which indicates that the MoSe$_2$/TiO$_2$ composite exhibits a n-type character. As evident from Fig. S6(f) (ESI†), in a separate I–V measurement at 30 °C, when a MoSe$_2$/TiO$_2$ (2 : 1) device was exposed to DMF and NH$_3$, an increase in current level was observed at a fixed voltage, thereby indicating that the composites exhibit n-type conductivity.[45] These changes in resistance
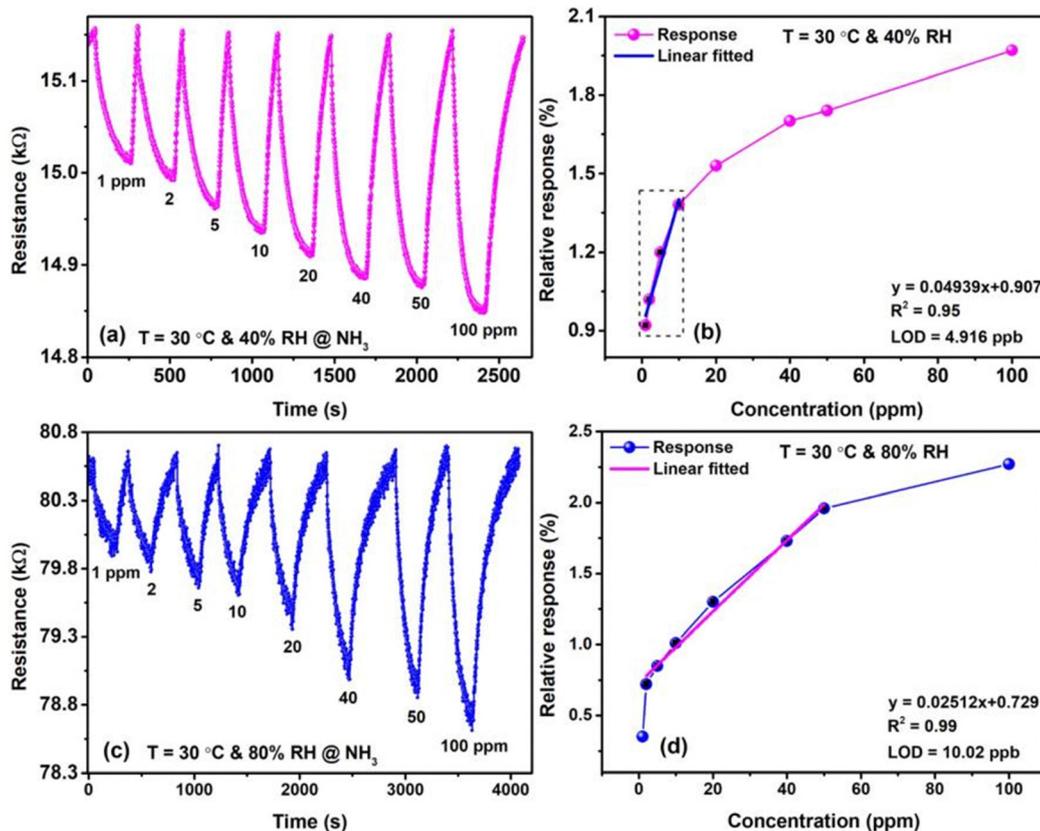
Fig. 3 (a) and (c) Response transient curves for the MoSe$_2$/TiO$_2$ (2 : 1) sensor exposed to various concentrations of NH$_3$ ranging from 1 to 100 ppm at 30 °C and relative humidity (RH) levels of 40% and 80%. (b) and (d) Relative response *versus* NH$_3$ concentration curves at 40% and 80% RH.

in response to different analytes serve as a basis for their detection.

Prior to conducting detailed sensing experiments, a representative measurement was performed at 30 °C and 40% relative humidity (RH) with 1 ppm of NH$_3$, as shown in Fig. 3 panel (a). The resistance of the device in air (R_a) decreased from 15.16 kΩ to 15.01 kΩ when exposed to NH$_3$ (R_g). This change in resistance allows for the calculation of various sensor parameters. Specifically, the absolute change in resistance in the presence of gas molecules is defined as $\Delta R = R_g - R_a$. The relative response, expressed as a percentage, is calculated using the formula $[\Delta R/R_a] \times 100$. The sensor response time ($t_{response}$) is defined as the duration required for the sensor to reach 90% of its maximum response upon exposure to the target gas, while the recovery time ($t_{recovery}$) is the time taken to return to a response value that is 10% above the maximum sensor response. A comparative analysis of the sensing performance between five different devices—MoSe$_2$, TiO$_2$, MoSe$_2$/TiO$_2$ (1 : 1), MoSe$_2$/TiO$_2$ (1 : 2), and MoSe$_2$/TiO$_2$ (2 : 1) composites, is illustrated in Fig. 3(a) and (c) and Fig. S7 (ESI†). Fig. S7a (ESI†) shows that the MoSe$_2$ sensor exhibits a 0.9% response at 20 ppm gas concentration under 40% humidity at room temperature. Fig. S7b (ESI†) represents the TiO$_2$ sensor, where the lower intrinsic conductivity of TiO$_2$ at room temperature might have contributed to the unstable response. However, the MoSe$_2$/TiO$_2$

(1 : 1) and MoSe$_2$/TiO$_2$ (1 : 2) composites exhibited unstable signals when exposed to NH$_3$ gas, as shown in Fig. S7c and d (ESI†). This instability can be attributed to the improper balance between the components in the composite. The higher proportion of TiO$_2$ in these ratios may have hindered the active sites required for NH$_3$ adsorption and disrupted the charge transfer mechanism between MoSe$_2$ and TiO$_2$, leading to signal fluctuations. Additionally, the lower intrinsic conductivity of TiO$_2$ at room temperature, particularly in higher TiO$_2$ ratios, might have further contributed to the unstable response. In Fig. 3, these measurements were conducted for 1 ppm of NH$_3$ at both room temperature and at 40% and 80% RH. The advantages of employing composite materials over pure MoSe$_2$ or TiO$_2$ are evident, attributed to factors such as increased specific surface area, the presence of defects, oxygen vacancies, and the synergistic effects that arise from composite formation.[35,53,54] Fig. 3(a) and (c) present the response transients at 40% and 80% RH, respectively. The baseline resistance of the sensor varies between the two RH conditions (40% and 80% RH) due to the presence of water molecules in the atmosphere. At higher humidity levels, more water molecules are adsorbed on the surface of the sensor, which can contribute to an increase in the baseline resistance due to the formation of a resistive water layer. This phenomenon is common in semiconducting metal oxides and TMDC-based sensors, where the adsorption of water

molecules leads to changes in charge carrier density, impacting the sensor's conductivity. Panels Fig. 3(b) and (d) depict the relative response against NH$_3$ concentration. The response showed a linear relationship from 1 to 100 ppm, with saturation observed at higher concentrations for both RH levels. The fitting curves for the sensor response *versus* NH$_3$ concentration demonstrated strong linear correlations, with coefficients of determination (R^2) of 0.95 and 0.99 for 40% and 80% RH, respectively. From the linear fitting, the theoretical limit of detection (LOD) can be calculated using the equation known as sensitivity, defined as three times the standard deviation (σ) of sensor noise divided by the slope (s) of the fitted curve, as expressed in eqn (2).

$$LOD = \frac{3\sigma}{s} \qquad (2)$$

For ammonia (NH$_3$), the limit of detection (LOD) was determined to be ~4.91 ppb at 40% relative humidity (RH) and ~10.02 ppb at 80% RH. The sensitivity of the sensor, represented by the slope (s), was calculated to be 0.049 per ppm at 40% RH and 0.02 per ppm at 80% RH. Notably, the response of the composite sensor exhibited minimal variation as humidity levels increased, highlighting the importance of response stability and consistency in practical sensor applications. Stability and repeatability, along with long-term durability, are critical parameters for assessing gas sensor performance. The sensor's response to 5, 10, and 40 ppm NH$_3$ is illustrated in Fig. S8(c) (ESI†), where the device demonstrated consistent performance across multiple cycles with negligible changes in response transients. Recovery times varied, being shorter or longer than the response times at 40% and 80% RH.

To evaluate sensor reproducibility, we prepared two additional sensors using the same methodology. The response transient curves for these devices, which are MoSe$_2$/TiO$_2$ (2:1) sensors, are presented in Fig. S8(a) and (b) (ESI†). These figures represent the response to increasing NH$_3$ concentrations from 1 ppm to 100 ppm and decreasing concentrations from 100 ppm to 1 ppm. Both sensors were tested under 40% and 80% humidity at room temperature, demonstrating consistent performance under varying humidity conditions. Over a continuous testing period of 10 weeks, the MoSe$_2$/TiO$_2$ (2:1) composite sensor was exposed to 10 ppm NH$_3$, as shown in Fig. S8(d) (ESI†). Remarkably, there was no significant decrease in response, with only slight variation, indicating excellent long-term durability and stability. As clearly seen, the sensing curves in Fig. S8d (ESI†) were constructed based on measurements taken at different time intervals-such as the 1st week, 2nd week, 3rd week, and so on. These measurements were then compiled into a single figure to provide a comprehensive overview of the sensor's performance over time. The variations observed in the curves can be attributed to slight fluctuations in humidity and temperature during each set of measurements conducted under real-world conditions. Additionally, the gas sensing experiments were carried out using a homemade gas sensing setup. In this setup, gas is injected using a syringe, which may introduce small variations in gas concentration due to manual handling.

While we strive for precision, minor human error and variations in gas injection can occur, leading to slight differences in the sensing curves. Nevertheless, the robustness, accuracy, and reliability of the MoSe$_2$/TiO$_2$ (2:1) sensor were further demonstrated by consistent responses across all tested conditions, reinforcing confidence in its ability to deliver accurate measurements in real-world applications. As depicted in Fig. 4 panels "a" and "b", the response time remained consistent at 150 s across both humidity levels 40% and 80%, while recovery times were 37 s and 110 s, respectively. The response time under higher humidity (80% RH) is generally higher compared to lower humidity (40% RH). This is because the water molecules adsorbed on the surface of the sensor may act as a barrier, slowing down the adsorption of ammonia (NH$_3$) molecules onto the active sites of the composite material. Water molecules can compete with ammonia for adsorption sites, leading to slower response times. Conversely, at lower humidity levels (40% RH), fewer water molecules are present, allowing NH$_3$ molecules to interact more freely with the sensor's surface, thus reducing the response time. Selectivity and specificity are also vital for high-performance chemiresistive gas sensors. The MoSe$_2$/TiO$_2$ (2:1) composite sensor was tested at 30 °C and 40% RH against a variety of volatile organic compounds (VOCs), including NH$_3$, N,N-dimethylformamide (DMF), acetone, ethanol, methanol, propanol, formaldehyde (FMD), and N-methyl-2-pyrrolidone (NMP), each at a concentration of 150 ppm, excluding NH$_3$ and DMF. The sensor exhibited significantly higher responses to NH$_3$ ($\approx$2.6%) and DMF ($\approx$2.4%) at 150 ppm compared to the other gases, underscoring its high selectivity towards NH$_3$ and DMF, as shown in Fig. 4(c).

Because the MoSe$_2$/TiO$_2$ (2:1) composite sensor is more sensitive to DMF, we evaluated its performance at low concentrations and compared it with other sensors, as shown in Fig. S9 (ESI†). One can see that the MoSe$_2$ signal is visible, but TiO$_2$ does not show any signal at room temperature. Additionally, no signal is observed for the MoSe$_2$/TiO$_2$ (1:1) and MoSe$_2$/TiO$_2$ (1:2) composites with DMF. The reason that the TiO$_2$, MoSe$_2$/TiO$_2$ (1:1), and MoSe$_2$/TiO$_2$ (1:2) composites do not show any significant signal in DMF can be attributed to several factors. Firstly, TiO$_2$ has low intrinsic conductivity at room temperature, which limits its ability to respond to DMF molecules, particularly without external stimuli such as elevated temperatures. In the case of MoSe$_2$/TiO$_2$ (1:1) and (1:2) composites, the higher proportion of TiO$_2$ in these composites may have reduced the number of active sites available for DMF adsorption on the MoSe$_2$ surface. This imbalance in the composite structure likely disrupts the charge transfer process between MoSe$_2$ and TiO$_2$, making it less effective in detecting DMF. Furthermore, the presence of a higher amount of TiO$_2$ in these ratios might hinder the overall sensor response by diluting the electroactive MoSe$_2$ component, which is primarily responsible for detecting DMF molecules. As a result, no significant signal is observed for these composites at room temperature.

Interestingly, the relative response of the MoSe$_2$/TiO$_2$ (2:1) composite sensor with varying levels of DMF ranging is strikingly different (see Fig. 5 and Fig. S10, ESI†). The response
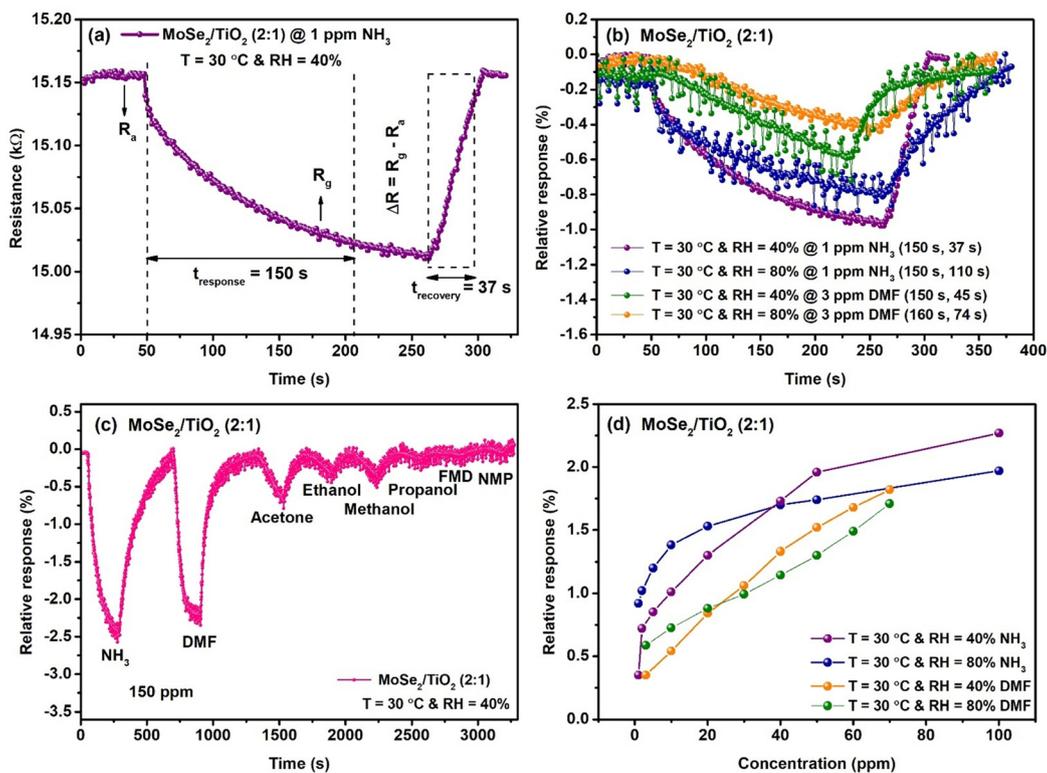
Fig. 4 (a) A representative response-recovery transient for the MoSe$_2$/TiO$_2$ (2 : 1) sensor with 1 ppm ammonia at 30 °C and 40% RH. (b) Sensing response of the MoSe$_2$/TiO$_2$ (2 : 1) composite sensor for different humidities and different analytes. (c) Selectivity tests for the MoSe$_2$/TiO$_2$ (2 : 1) composite sensor to various gases at room temperature. (d) Relative response vs concentration in different humidities and different analytes (NH$_3$ and DMF).
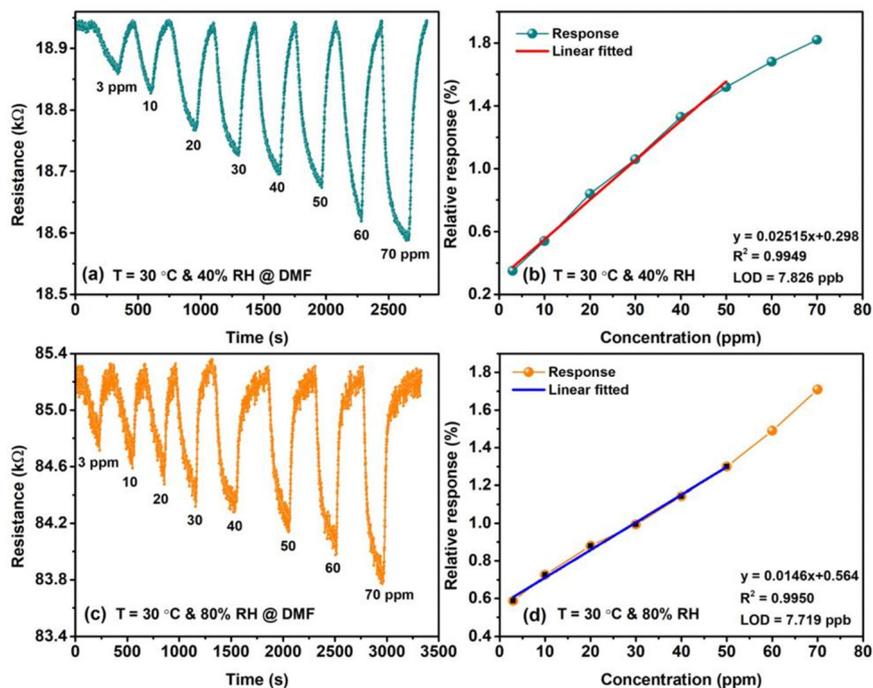

Fig. 5 (a), (c) Response transient curves for the MoSe$_2$/TiO$_2$ (2 : 1) sensor when exposed to varying concentrations of DMF from 3 to 70 ppm at 30 °C and relative humidity (RH) levels of 40% and 80%. (b) and (d) Relative response versus DMF concentration curves at 40% and 80% RH.

exhibited a linear variation from 3 to 70 ppm and tended to saturate at higher concentrations at both RH (40% and 80%) levels. The fitting curves of the sensor response *versus* the DMF concentration (ppm) displayed a good linear correlation with $R^2 = 0.99$, for different humidity levels. From linear fitting, one can calculate the theoretical LOD to be $\sim$7.82 and $\sim$7.71 ppb at RH 40% and RH 80%, respectively. To assess the reproducibility of the sensors, we fabricated two additional $MoSe_2/TiO_2$ (2:1) sensors using the same methodology. The response transient curves for these sensors are shown in Fig. S10(a) and (b) (ESI†). These figures illustrate the sensor responses to increasing DMF concentrations, ranging from 3 ppm to 70 ppm, and then decreasing concentrations from 70 ppm to 3 ppm. Both sensors were evaluated under 40% and 80% humidity at room temperature, demonstrating consistent and reliable performance across varying humidity levels. Fig. S10(c) (ESI†) presents repeatability cycles for the $MoSe_2/TiO_2$ (2:1) composite sensor response to 20 and 40 ppm DMF concentration. Over a continuous testing period of 10 weeks, the $MoSe_2/TiO_2$ (2:1) composite sensor was exposed to 10 ppm DMF, as shown in Fig. S10(d) (ESI†). Remarkably, there was no significant diminution in response, with only slight variation, indicating excellent long-term durability and stability. The robustness, accuracy, and reliability of the $MoSe_2/TiO_2$ (2:1) sensor were further demonstrated by consistent responses across all tested conditions, reinforcing confidence in its ability to deliver accurate measurements in real-world applications. Similar to NH_3 sensing experiments, the measurements for DMF sensing were also taken at regular intervals such as the 1st week, 2nd week, 3rd week, and so on. These results were compiled into a single figure to provide a comprehensive view of the sensor's performance over time. The slight variations observed can be attributed to environmental factors such as fluctuations in humidity and temperature. As with the ammonia experiments, the gas was injected manually using a syringe in a homemade gas sensing setup, which may have introduced minor variations in gas concentration. Despite these small inconsistencies, the sensor's performance remained consistent, further demonstrating its reliability for real-world applications. Fig. 4(b) shows the DMF response time (160 s, and 150 s) and recovery time (74 s, 45 s) of different humidity conditions 40% and 80%. Fig. 4(d) shows the relative responses of four different composite sensors under varying humidity and analytes. We observed that the highest response occurs with NH_3 when the room temperature is at 40% humidity, indicating that the sensor performs best under these conditions.

3.3 Density functional theory studies

3.3.1 Structural and electronic properties. We explored the absorption behaviour of NH_3 and DMF on the $MoSe_2/TiO_2$ heterostructure, vertically stacked by $MoSe_2$ and TiO_2 monolayers with an interlayer distance of 3.61 Å. The $2 \times 1 \times 1$ supercell of the $MoSe_2$ monolayer and $2 \times 2 \times 1$ supercell of the TiO_2 monolayer was used to construct the $MoSe_2/TiO_2$ heterostructure, which consists of 16 Mo atoms, 32 Se atoms, 16 Ti and 32 O atoms. The $MoSe_2/TiO_2$ heterostructure has optimized

Table 1 The adsorption energy (E_{ads}) and the optimum distance between gas molecules and the adsorbent (d) of the heterostructure

Gas species	Adsorption site	E_{ads} (eV)	Optimum distance d (Å)
NH_3	Below-$MoSe_2$	−0.12	3.45
	top-TiO_2	0.27	2.98
DMF	below-$MoSe_2$	−0.09	3.25
	top-TiO_2	−0.05	2.76

lattice parameters a and b, which are 13.26 Å and 11.49 Å, respectively. Notably, the heterostructure exhibits approximately 3% lattice mismatch. Top and side views of the optimized $MoSe_2/TiO_2$ heterostructure are shown in Fig. S11(a) and (b) (ESI†). To examine the affinity of the gas molecules, we investigated the behavior of the NH_3 and DMF on various sites of the $MoSe_2/TiO_2$ heterostructure. These distinct sites were labelled as "below-$MoSe_2$ surface" and "top-TiO_2" surface", as shown in Fig. S12(a)–(d) (ESI†).

We also studied the adsorption behavior of NH_3 and DMF on these different surfaces of heterostructure and the value of relevant adsorption energy and optimum distance, as illustrated in Table 1.

We determined the adsorption energy (E_{ads}) using the below equation. The equation can be represented as:

$$E_{ads} = E_{hetero+molecule} - E_{hetero} - E_{molecule}$$

where $E_{hetero+molecule}$ represents the entire energy of the heterostructure, E_{hetero} indicates the energy of the $MoSe_2/TiO_2$ heterostructure, and $E_{molecule}$ represents the energy of the NH_3 molecule and DMF.

We investigated the adsorption energy (E_{ads}) of NH_3 molecules and DMF at various adsorption sites on the $MoSe_2/TiO_2$ heterostructure. NH_3 exhibits the lowest E_{ads} value (−0.12 eV) and is most favourable at the below-$MoSe_2$ surface, as compared to the top-TiO_2 surface. Notably, the E_{ads} value for DMF at both the below-$MoSe_2$ and top-TiO_2 sites is negative, indicating spontaneous and heat-releasing adsorption mechanisms. DMF exhibits lowest absorption energy (−0.09 eV) at the below-$MoSe_2$ surface, illustrated in Table 1, highlighting its strong interaction with this substrate compared to the top-TiO_2 surface.

To deeply examine the impact of the NH_3 and DMF adsorption on the $MoSe_2/TiO_2$ heterostructures, we calculated the electronic band structure, which revealed that the heterostructure exhibits an indirect band gap of (0.31 eV), significantly increased by approximately (0.09 eV) after NH_3 adsorption on the below-$MoSe_2$ surface, as shown in Fig. 6(a) and (c). However, this change is attributed to the heterostructure's quantum confinement effects, surface dipoles, and charge redistribution. Additionally, we examined the projected density of states (PDOS) for each constituent atom. Notably, Mo and Ti atoms predominantly influence the electronic state near the Fermi level in the heterostructure, depicted in Fig. 6(b) and (d).

Furthermore, we examined the absorption behaviour of DMF on the below-$MoSe_2$ surface, and the bandgap slightly increased (0.36 eV), as depicted in Fig. S13(a) (ESI†).
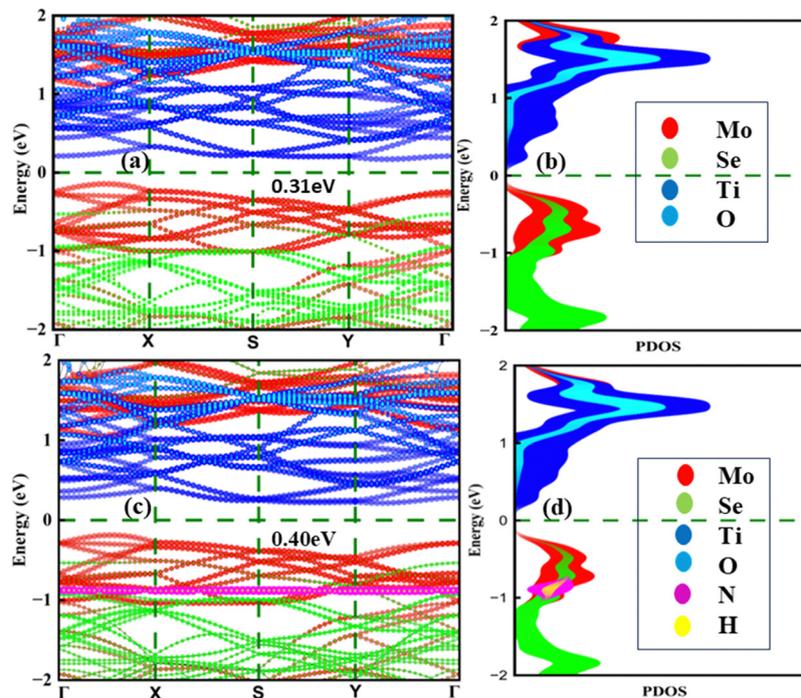
Fig. 6 (a) and (c) Electronic band structure and (b) and (d) projected density of state of the MoSe$_2$/TiO$_2$ heterostructure and after NH$_3$ adsorbed on the heterostructure, respectively, using the GGA + PBE method.

Additionally, we computed the projected density of states (PDOS) as shown in Fig. S13(b) (ESI†), highlighting the intricate interaction between the constituent atom and adsorbate, emphasizing the importance of the heterostructure modulating the electronic behaviour of materials.

We analyzed the Bader charge of NH$_3$ and DMF on the MoSe$_2$/TiO$_2$ heterostructure. A positive value of Bader charge (0.01e) is observed, confirming physisorption,[55] highlighting the high sensitivity of the MoSe$_2$ surface toward the NH$_3$ molecule,[53,56] as shown in Fig. 7(a) and (b). The small negative value of Bader charge ($-0.09e$) of DMF indicates a slight electron accumulation on the MoSe$_2$ surface as depicted in Fig. 7(c) and (d), affecting the electronic properties of the heterostructure, crucial for gas sensing application.[57]

The charge transfer influences the surface charge distribution, impacting the material's overall reactivity and interactions with other adsorbates. The amount of charge transfer indicates the exchange of electrons within this system. The Bader charge analysis obtained the charge transfer (Q) outcomes, while a positive value of NH$_3$ (electron are transfer from the monolayer to NH$_3$ molecule) and a negative value of DMF (electron are transfer from DMF to the monolayer) suggests depletion and accumulation, respectively.[57] The charge transfer was determined through Bader analysis, as shown in Table 2. Based on the adsorption energy and Bader charge analysis, we conclude that the below-MoSe$_2$ surface of the heterostructure exhibits strong adsorption capability for NH$_3$ and DMF.

3.4 Sensing mechanism and discussion

The experimental findings demonstrated that the MoSe$_2$/TiO$_2$ (2:1) hybrid material exhibited enhanced sensing properties, particularly as an NH$_3$ gas sensor. The sensing mechanism for
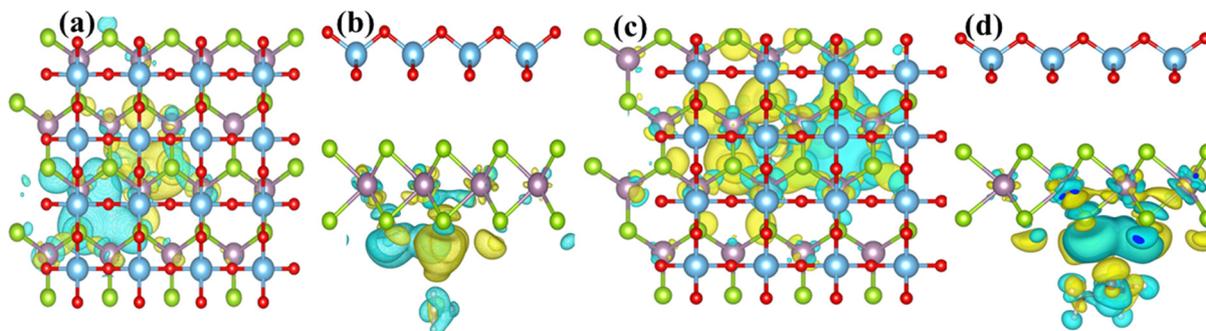

Fig. 7 (a) and (c) Top and (b) and (d) side view of the charge density difference of NH$_3$ and DMF absorption at the below-MoSe$_2$ site of the heterostructure, respectively; hence, cyan and yellow colours represent the depletion and accumulation of charges, respectively.

Table 2 The net Bader charge on NH_3 and DMF at below-$MoSe_2$ sites of the heterostructure

Gas species	Atom	$Q_{transfer}$ (e)	Bader charge (e)
NH_3	N	−1.25	0.01
	H	0.43	
	H	0.43	
	H	0.40	
DMF	O	−0.85	−0.09
	N	−0.59	
	C	−0.32	
	C	−0.34	
	C	0.73	
	H	0.18	
	H	0.20	
	H	0.19	
	H	0.18	
	H	0.19	
	H	0.22	
	H	0.15	

$MoSe_2/TiO_2$ (2:1) based chemiresistive sensors relies on variations in electrical conductance caused by the adsorption and subsequent charge transfer between gas molecules and the material's surface. As discussed earlier, the $MoSe_2/TiO_2$ (2:1) sensor had the most pronounced response (negative relative response) to NH_3. Additionally, density functional theory (DFT) simulations were employed to assess the adsorption energy (E_{ads}) and the charge transfer (e) for reducing gases like NH_3. The computed values for NH_3 were E_{ads} = −0.12 eV and e = 0.01e. The negative adsorption energy and significant charge transfer from the $MoSe_2$ surface indicate a spontaneous,

exothermic physisorption process. The operating principle of the $MoSe_2/TiO_2$ sensor is based on semiconductor behavior, where the surface resistance is regulated by the adsorption of gas molecules. When NH_3 molecules adsorb and desorb from the $MoSe_2/TiO_2$ surface, it leads to a measurable change in resistance, enabling the detection of NH_3.[58] In semiconductors, O_2 molecules may capture free electrons to form oxygen ions (such as O_2^-, O^-, or O_2^{2-}). This surface reaction can be described by the following equations:

$$O_{2(air)} \rightarrow O_{2(ads)}, \qquad (3)$$

$$O_{2(ads)} + e^- \rightarrow O_{2(ads)}^-, \qquad (4)$$
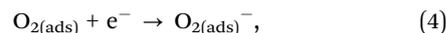
Based on the structural design of the sensing material and theoretical principles, when the $MoSe_2/TiO_2$ sensor is exposed to reducing gases like NH_3, the surface-adsorbed oxygen species interact with NH_3 molecules, leading to the production of N_2, H_2O, and the release of free electrons into the conduction band. These electrons recombine with holes, which lowers the Schottky barrier height and reduces the thickness of the electron depletion layer (EDL). As a result, the sensor experiences a decrease in resistance.

$$4NH_3 + 3O_2^- \rightarrow 2N_2 + 6H_2O + 3e^- \qquad (5)$$
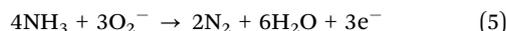
The $MoSe_2/TiO_2$ surface shows a distinct response to oxygen and ammonia gases. Both $MoSe_2$ and TiO_2 exhibit n-type semiconductor behavior, with TiO_2 having a bandgap of 3.2 eV and a work function of 5.2 eV (anatase phase).[59] In contrast, n-type $MoSe_2$ has a bandgap of 1.3 eV and a work function of
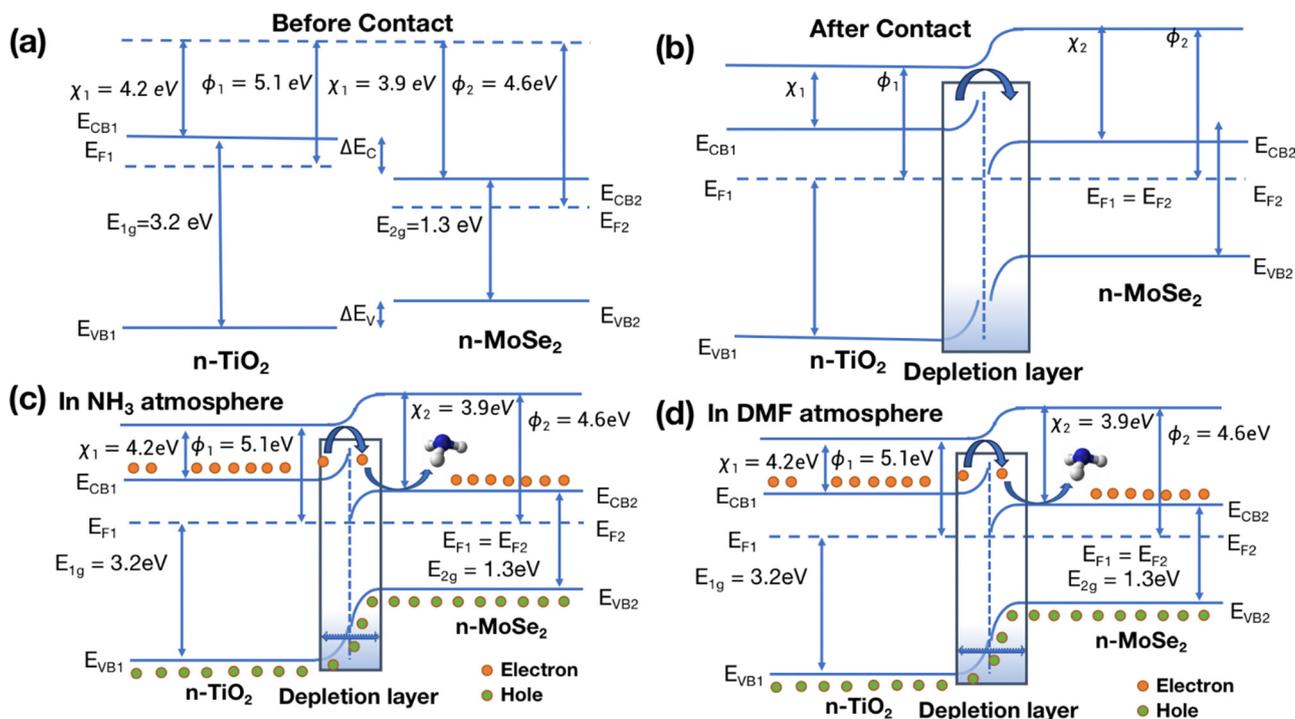

Fig. 8 (a) and (b) Simulated energy band diagram before and after contact and schematic showing the NH_3 sensing mechanism (c) and (d) in the NH_3 and DMF gas atmosphere, for the $MoSe_2/TiO_2$ heterojunction.

4.6 eV.[60] The formation of a composite leads to the creation of an n–n type heterostructure. As illustrated in Fig. 8(a), the lower work function of $MoSe_2$ results in its Fermi level being higher than that of TiO_2. When the two materials come into contact, electrons are transferred from $MoSe_2$ (with a lower work function) to TiO_2 (with a higher work function), resulting in the development of a depletion layer at the junction until the Fermi levels of both materials equalize as shown in Fig. 8(b). Electrons in the accumulation layer of TiO_2 combine with oxygen from the environment to form O_2^- ions. When the $MoSe_2/TiO_2$ heterostructure is exposed to NH_3, the gas interacts with the adsorbed oxygen species, releasing electrons into the $MoSe_2$ conduction band. This leads to an increase in electron concentration in $MoSe_2$ and a reduction in hole concentration in TiO_2, thereby thinning the depletion layer and reducing the sensor's resistance, as shown in Fig. 8(c). A similar decrease in resistance (negative relative response) is observed when the sensor is exposed to DMF, showing a significant response, second only to NH_3.

$$21O_2^- + 4(C_3H_7NO) \rightarrow 12CO_2 + 14H_2O + 4NO_2 + 21e^-$$
(6)
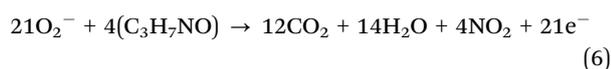
When the sensor is exposed to DMF vapors, the DMF molecules interact with the oxygen species adsorbed on the sensor's surface, leading to the release of electrons into the conduction band. This interaction increases the electron concentration and enhances the hole concentration in the n–n type junctions of the $MoSe_2/TiO_2$ composite. Consequently, as shown in Fig. 8(d), the depletion layer becomes thinner, resulting in a decrease in the sensor's resistance.

4. Conclusion

In this study, $MoSe_2/TiO_2$ composite-based sensors were successfully fabricated and tested for gas sensing at room temperature. Both experimental and theoretical analyses demonstrated selective and rapid responses to NH_3 and DMF compared to other analytes. The sensor exhibited a significantly higher response, approximately 85% for NH_3 and 80% for DMF, compared to other gases tested. Adsorption characteristics revealed a feasible exothermic physisorption process for both gases, supported by the negative adsorption energy values. DFT calculations further confirmed these results, with the computed bandgap of the $MoSe_2/TiO_2$ heterostructure slightly increasing from 0.31 eV to 0.36 eV after DMF adsorption, and to 0.40 eV after NH_3 adsorption, indicating improved electronic properties for gas sensing applications. Bader charge analysis revealed a charge transfer of $0.01e$ from NH_3 to the $MoSe_2/TiO_2$ heterostructure, enhancing its conductivity and sensitivity. The Bader charge value of $-0.09e$ for DMF indicated weak physisorption, with minimal electron accumulation on the $MoSe_2$ surface, affecting conductivity and overall reactivity. These results suggest that the $MoSe_2/TiO_2$ composite is well-suited for reversible gas sensing. The modulated band gap,

alongside the negative adsorption energy results, underscores the potential of the $MoSe_2/TiO_2$ composite for NH_3 and DMF detection. The sensor demonstrated impressive room-temperature performance, with calculated limits of detection for NH_3 of approximately 4.91 ppb at 40% relative humidity and 10.02 ppb at 80% relative humidity, with sensitivity slopes of 0.049 and 0.02 per ppm, respectively. For DMF, the limits of detection were 7.82 ppb at 40% RH and 7.71 ppb at 80% RH. The sensor showed response times of 150 s and 160 s for DMF at 40% and 80% RH, respectively, with recovery times of 45 s and 74 s. For NH_3, the response time was consistent at 150 s under both humidity conditions, while the recovery times were 37 s at 40% RH and 110 s at 80% RH.

Moreover, the sensor exhibited stable and repeatable performance during long-term durability assessments. The ability to operate at room temperature without requiring additional recovery mechanisms confirms the practical usability of the device. These findings strongly support the potential of $MoSe_2/TiO_2$ heterostructures as highly efficient and selective sensors for NH_3 and DMF detection in ambient conditions.

Author contributions

Virendra Singh Choudhary: conceptualization, methodology, investigation, formal analysis, writing – original draft, visualization. Ramandeep & Ashok Kumar: investigation, methodology, DFT calculations, data curation. C. S. Yadav: characterization, XPS data acquisition. Sandeep Sharma: manuscript editing. Joel Garcia: manuscript editing. Surender Kumar Sharma: supervision, manuscript editing, final review.

Data availability

The data supporting this article have been included as part of the ESI.†

Conflicts of interest

There are no conflicts to declare.

Acknowledgements

References

1 S. Hong, M. Wu, Y. Hong, Y. Jeong, G. Jung, W. Shin, J. Park, D. Kim, D. Jang and J. H. Lee, FET-type gas sensors: A review, *Sens. Actuators, B*, 2021, **330**, 129240.
2 W. Li, Y. Zhang, X. Hao, Y. Zhang, X. Yang, X. Liang, F. Liu, X. Yan, S. Zhang and G. Lu, Nafion-based methanol gas

sensor for fuel cell vehicles, *Sens. Actuators, B*, 2020, **311**, 127905.

3 L. Petani, L. Koker, J. Herrmann, V. Hagenmeyer, U. Gengenbach and C. Pylatiuk, Recent Developments in Ozone Sensor Technology for Medical Applications, *Micromachines*, 2020, **11**, 624.

4 J. van den Broek, D. Klein Cerrejon, S. E. Pratsinis and A. T. Güntner, Selective formaldehyde detection at ppb in indoor air with a portable sensor, *J. Hazard. Mater.*, 2020, **399**, 123052.

5 A. Bhardwaj, I. H. Kim, L. Mathur, J. Y. Park and S. J. Song, Ultrahigh-sensitive mixed-potential ammonia sensor using dual-functional $NiWO_4$ electrocatalyst for exhaust environment monitoring, *J. Hazard. Mater.*, 2021, **403**, 123797.

6 Y. Zhou, R. Zhang, X. She, J. Li, H. Zhao, Y. Wang, Y. Chen, L. Xie, C. Zou and X. Li, Alkalized Cellulose Nanofiber-Interweaved PEDOT:PSS Thin-Film Sensors via Layer-by-Layer Spraying Assembly for Ultrafast Molecular Ammonia Detection, *ACS Appl. Mater. Interfaces*, 2023, **15**, 53802–53814.

7 M. Mayer and A. J. Baeumner, A Megatrend Challenging Analytical Chemistry: Biosensor and Chemosensor Concepts Ready for the Internet of Things, *Chem. Rev.*, 2019, **119**, 7996–8027.

8 C. Jia, S. Batterman and C. Godwin, VOCs in industrial, urban and suburban neighborhoods—Part 2: Factors affecting indoor and outdoor concentrations, *Atmos. Environ.*, 2008, **42**, 2101–2116.

9 J. J. Ye, S. S. Wang, Y. Fang, X. J. Zhang and C. Y. Hu, Ambient air pollution exposure and risk of chronic kidney disease: A systematic review of the literature and meta-analysis, *Environ. Res.*, 2021, **195**, 110867.

10 F. Y. Al-Aboosi, M. M. El-Halwagi, M. Moore and R. B. Nielsen, Renewable ammonia as an alternative fuel for the shipping industry, *Curr. Opin. Chem. Eng.*, 2021, **31**, 100670.

11 K. Wetchakun, T. Samerjai, N. Tamaekong, C. Liewhiran, C. Siriwong, V. Kruefu, A. Wisitsoraat, A. Tuantranont and S. Phanichphant, Semiconducting metal oxides as sensors for environmentally hazardous gases, *Sens. Actuators, B*, 2011, **160**, 580–591.

12 H. Tai, S. Wang, Z. Duan and Y. Jiang, Evolution of breath analysis based on humidity and gas sensors: Potential and challenges, *Sens. Actuators, B*, 2020, **318**, 128104.

13 S. Singh, J. Deb, U. Sarkar and S. Sharma, $MoSe_2$ Crystalline Nanosheets for Room-Temperature Ammonia Sensing, *ACS Appl. Nano Mater.*, 2020, **3**, 9375–9384.

14 Y. Li, S. Zhang and D. Song, A Luminescent Metal–Organic Framework as a Turn-On Sensor for DMF Vapor, *Angew. Chem., Int. Ed.*, 2013, **52**(2), 710–713, DOI: **10.1002/anie.201207610**.

15 Q. Chen, J. Li, W. Fu, Y. Yang, W. Zhu and J. Zhang, Detection of N, N-dimethylformamide vapor down to ppb level using electrospunInYbO nanofibers field-effect transistor, *Sens. Actuators, B*, 2020, **323**, 128676.

16 J. Baranwal, B. Barse, G. Gatto, G. Broncova and A. Kumar, Electrochemical Sensors and Their Applications: A Review, *Chemosensors*, 2022, **10**, 363.

17 R. Zhang, Y. Wang, J. Li, H. Zhao, Y. Wang and Y. Zhou, Mesoporous cellulose nanofibers-interlaced PEDOT:PSS hybrids for chemiresistive ammonia detection, *Microchim. Acta*, 2022, **189**, 308.

18 R. Owyeung, M. Panzer and S. R. Sonkusale, Colorimetric gas sensing washable threads for smart textiles, *Sci. Rep.*, 2019, **9**(1), 5607.

19 Y. Zhou, Y. Wang, Y. Wang, H. Yu, R. Zhang, J. Li, Z. Zang and X. Li, MXene $Ti_3C_2T_x$-Derived Nitrogen-Functionalized Heterophase TiO_2 Homojunctions for Room-Temperature Trace Ammonia Gas Sensing, *ACS Appl. Mater. Interfaces*, 2021, **13**, 56485–56497.

20 H. Zhao, J. Li, X. She, Y. Chen, M. Wang, Y. Wang, A. Du, C. Tang, C. Zou and Y. Zhou, Oxygen Vacancy-Rich Bimetallic Au@Pt Core–Shell Nanosphere-Functionalized Electrospun $ZnFe_2O_4$ Nanofibers for Chemiresistive Breath Acetone Detection, *ACS Sens.*, 2024, **9**, 2183–2193.

21 C. Yu, J. Liu, H. Zhao, M. Wang, J. Li, X. She, Y. Chen, Y. Wang, B. Liu, C. Zou, Y. He and Y. Zhou, Sensitive Breath Acetone Detection Based on α-Fe_2O_3 Nanoparticles Modified WO_3 Nanoplate Heterojunctions, *IEEE Trans. Instrum. Meas.*, 2024, **73**, 9513908.

22 K. Wu, M. Debliquy and C. Zhang, Room temperature gas sensors based on Ce doped TiO_2 nanocrystals for highly sensitive NH3 detection, *Chem. Eng. J.*, 2022, **444**, 136449.

23 V. Schroeder, S. Savagatrup, M. He, S. Lin and T. M. Swager, Carbon nanotube chemical sensors, *Chem. Rev.*, 2019, **119**, 599–663.

24 X. Liu, T. Ma, N. Pinna and J. Zhang, Two-Dimensional Nanostructured Materials for Gas Sensing, *Adv. Funct. Mater.*, 2017, **27**, 1702168.

25 H. Y. Li, S. N. Zhao, S. Q. Zang and J. Li, Functional metal–organic frameworks as effective sensors of gases and volatile compounds, *Chem. Soc. Rev.*, 2020, **49**, 6364–6401.

26 Y. Zhou, G. Liu, X. Zhu and Y. Guo, Ultrasensitive NO_2 gas sensing based on rGO/MoS_2 nanocomposite film at low temperature, *Sens. Actuators, B*, 2017, **251**, 280–290.

27 S. Singh, S. Sharma, R. C. Singh and S. Sharma, Hydrothermally synthesized MoS_2-multi-walled carbon nanotube composite as a novel room-temperature ammonia sensing platform, *Appl. Surf. Sci.*, 2020, **532**, 147373.

28 S. Singh, J. Deb, U. Sarkar and S. Sharma, MoS_2/WO_3 Nanosheets for Detection of Ammonia, *ACS Appl. Nano Mater.*, 2021, **4**, 2594–2605.

29 S. Sharma, A. Kumar, N. Singh and D. Kaur, Excellent room temperature ammonia gas sensing properties of n-MoS_2/p-CuO heterojunction nanoworms, *Sens. Actuators, B*, 2018, **275**, 499–507.

30 D. Zhang, C. Jiang, P. Li and Y. Sun, Layer-by-Layer Self-assembly of Co_3O_4 Nanorod-Decorated MoS_2 Nanosheet-Based Nanocomposite toward High-Performance Ammonia Detection, *ACS Appl. Mater. Interfaces*, 2017, **9**, 6462–6471.

31 Z. Pang, Z. Yang, Y. Chen, J. Zhang, Q. Wang, F. Huang and Q. Wei, A room temperature ammonia gas sensor based on cellulose/TiO_2/PANI composite nanofibers, *Colloids Surf., A*, 2016, **494**, 248–255.

32 H. Tai, Z. Duan, Z. He, X. Li, J. Xu, B. Liu and Y. Jiang, Enhanced ammonia response of Ti$_3$C$_2$T$_x$ nanosheets supported by TiO$_2$ nanoparticles at room temperature, *Sens. Actuators, B*, 2019, **298**, 126874.

33 N. Dogra, S. Gasso, A. Sharma, K. K. Sharma and S. Sharma, TiO2 decorated MXene nanosheets for high-performance ammonia gas sensing at room-temperature, *Surf. Interfaces*, 2024, **48**, 104290.

34 W. Buraso, V. Lachom, P. Siriya and P. Laokul, Synthesis of TiO$_2$ nanoparticles *via* a simple precipitation method and photocatalytic performance, *Mater. Res. Express*, 2018, **5**, 115003.

35 N. Dogra, S. S. Kushvaha and S. Sharma, Phase-Dependent Dual Discrimination of MoSe$_2$/MoO$_3$ Composites Toward *N,N*-Dimethylformamide and Triethylamine at Room Temperature, *ACS Sens.*, 2023, **8**, 3146–3157.

36 G. Kresse and J. Hafner, *Ab initio* molecular dynamics for liquid metals, *Phys. Rev. B: Condens. Matter Mater. Phys.*, 1993, **47**, 558–561.

37 D. Joubert, From ultrasoft pseudopotentials to the projector augmented-wave method, *Phys. Rev. B: Condens. Matter Mater. Phys.*, 1999, **59**, 1758–1775.

38 G. Kresse and J. Furthmüller, Efficiency of *ab initio* total energy calculations for metals and semiconductors using a plane-wave basis set, *Comput. Mater. Sci.*, 1996, **6**, 15–50.

39 P. E. Blöchl, Projector augmented-wave method, *Phys. Rev. B: Condens. Matter Mater. Phys.*, 1994, **50**, 17953–17979.

40 H. J. Monkhorst and J. D. Pack, Special points for Brillouin-zone integrations, *Phys. Rev. B*, 1976, **13**, 5188–5192.

41 S. S. El-Deen, A. M. Hashem, A. E. A. Ghany, S. Indris, H. Ehrenberg, A. Mauger and C. M. Julien, Anatase TiO$_2$ nanoparticles for lithium-ion batteries, *Ionics*, 2018, **24**, 2925–2934.

42 H. Tang, K. Dou, C. Kaun, Q. Kuang and S. Yang, MoSe$_2$ nanosheets and their graphene hybrids: synthesis, characterization and hydrogen evolution reaction studies, *J. Mater. Chem. A*, 2014, **2**, 360–364.

43 X. T. Tran, S. Poorahong and M. Siaj, One-pot hydrothermal synthesis and selective etching method of a porous MoSe 2 sand rose-like structure for electrocatalytic hydrogen evolution reaction, *RSC Adv.*, 2017, **7**, 52345–52351.

44 Y. Lai, W. Chen, Z. Zhang, Y. Gan, X. Yang and J. Li, Two-dimensional graphene-like MoSe$_2$ nanosheets anchored on hollow carbon nanofibers as a cathode catalyst for rechargeable Li–O$_2$ batteries, *RSC Adv.*, 2016, **6**, 19843.

45 S. Tongay, J. Zhou, C. Ataca, K. Lo, T. S. Matthews, J. Li, J. C. Grossman and J. Wu, Thermally driven crossover from indirect toward direct bandgap in 2D Semiconductors: MoSe$_2$ *versus* MoS$_2$, *Nano Lett.*, 2012, **12**, 5576–5580.

46 U. Balachandran and N. G. Eror, Raman spectra of titanium dioxide, *J. Solid State Chem.*, 1982, **42**, 276–282.

47 G. Eda, H. Yamaguchi, D. Voiry, T. Fujita, M. Chen and M. Chhowalla, Photoluminescence from chemically exfoliated MoS$_2$, *Nano Lett.*, 2011, **11**, 5111–5116.

48 X. Fan, P. Xu, D. Zhou, Y. Sun, Y. C. Li, M. A. T. Nguyen, M. Terrones and T. E. Mallouk, Fast and Efficient Preparation of Exfoliated 2H MoS$_2$ Nanosheets by Sonication-Assisted Lithium Intercalation and Infrared Laser-Induced 1T to 2H Phase Reversion, *Nano Lett.*, 2015, **15**, 5956–5960.

49 C. Tan, W. Zhao, A. Chaturvedi, Z. Fei, Z. Zeng, J. Chen, Y. Huang, P. Ercius, Z. Luo, X. Qi, B. Chen, Z. Lai, B. Li, X. Zhang, J. Yang, Y. Zong, C. Jin, H. Zheng, C. Kloc and H. Zhang, Preparation of Single-Layer MoS$_{2x}$Se$_{2(1−x)}$ and Mo$_x$W$_{1−x}$S$_2$ Nanosheets with High-Concentration Metallic 1T Phase, *Small*, 2016, **12**, 1866–1874.

50 Z. T. Shi, W. Kang, J. Xu, Y. W. Sun, M. Jiang, T. W. Ng, H. T. Xue, D. Y. W. Yu, W. Zhang and C. S. Lee, Hierarchical nanotubes assembled from MoS$_2$-carbon monolayer sandwiched superstructure nanosheets for high-performance sodium ion batteries, *Nano Energy*, 2016, **22**, 27–37.

51 H. Wang, D. Kong, P. Johanes, J. J. Cha, G. Zheng, K. Yan, N. Liu and Y. Cui, MoSe$_2$ and WSe$_2$ nanofilms with vertically aligned molecular layers on curved and rough surfaces, *Nano Lett.*, 2013, **13**, 3426–3433.

52 L. Pan, S. Wang, J.-J. Zou, Z.-F. Huang, L. Wang and X. Zhang, Ti^{3+}-defected and V-doped TiO$_2$ quantum dots loaded on MCM-41, *Chem. Commun.*, 2014, 50, 988.

53 S. Singh, J. Deb, U. Sarkar and S. Sharma, MoS$_2$/MoO$_3$ Nanocomposite for Selective NH$_3$ Detection in a Humid Environment, *ACS Sustain, Chem. Eng.*, 2021, **9**, 7328–7340.

54 S. Singh, J. Deb, J. V. Singh, U. Sarkar and S. Sharma, Highly Selective Ethyl Mercaptan Sensing Using a MoSe$_2$/SnO$_2$ Composite at Room Temperature, *ACS Appl. Mater. Interfaces*, 2022, **14**, 23916–23927.

55 J. Deb, B. Bhattacharya, D. Paul and U. Sarkar, Interaction of nitrogen molecule with pristine and doped graphyne nanotube, *Phys. E*, 2016, **84**, 330.

56 J. Shen, Z. Yang, Y. Wang, L. Xu, R. Liu and X. Liu, The gas sensing performance of borophene/MoS$_2$ heterostructure, *Appl. Surf. Sci.*, 2020, **504**, 144412.

57 J. A. Mehrez, S. Jiao, M. Zeng, N. Hu, T. Wang, J. Abdul-Aziz Mehrez, X. Chen, J. Yang, R. Liu, L. Xu, Y. Gonzá Lez-Alfaro and Z. Yang, MoTe$_2$/InN van der Waals heterostructures for gas sensors: a DFT study, *Phys. Chem. Chem. Phys.*, 2023, **25**, 28677.

58 P. X. Zhao, Y. Tang, J. Mao, Y. X. Chen, H. Song, J. W. Wang, Y. Song, Y. Q. Liang and X. M. Zhang, One-Dimensional MoS2-Decorated TiO2 nanotube gas sensors for efficient alcohol sensing, *J. Alloys Compd.*, 2016, **674**, 252–258.

59 M. Setvin, J. Hulva, G. S. Parkinson, M. Schmid and U. Diebold, Electron transfer between anatase TiO$_2$ and an O$_2$ molecule directly observed by atomic force microscopy, *Proc. Natl. Acad. Sci. U. S. A.*, 2017, **114**, E2556–E2562.

60 L. Zhou, Q. Mi, Y. Jin, T. Li and D. Zhang, Construction of MoO$_3$/MoSe$_2$ nanocomposite-based gas sensor for low detection limit trimethylamine sensing at room temperature, *J. Mater. Sci.: Mater. Electron.*, 2021, **32**, 17301–17310.